Electrosynthesis of iron-based metal-organic materials with bis(salicylic acid) derivatives

Sara Realista,[*[a]§] Ana R. Reis,[[a]§] Duarte Borralho,[[a]] Victoria Corregidor,[[b]] Luís C. Alves,[[b]] Sérgio Magalhães,[[c]] Telmo Nunes,[[d]] Ana S. Viana,[[a]] João Pires,[[a]] Ana M. Ferraria,[[e]] Ana M. Botelho do Rego[[e]] and Paulo N. Martinho[[a]]

[a] Centro de Química Estrutural, Institute of Molecular Sciences, Departamento de Química e Bioquímica, Faculdade de Ciências, Universidade de Lisboa, Campo Grande, Ed. C8, 1749-016 Lisboa, Portugal.
[b] C2TN,DECN,E.N.10 (km 139.7), Instituto Superior Técnico, Universidade de Lisboa, 2695-066 Bobadela, Portugal
[c] IPFN, Instituto de Plasmas e Fusão Nuclear, Campus Tecnológico e Nuclear, Instituto Superior Técnico, Universidade de Lisboa, Estrada Nacional 10, 2695-066 Bobadela LRS, Portugal.
[d] FCUL Microscopy Facility, Faculdade de Ciências, Universidade de Lisboa, Campo Grande, Ed. C2, 1749-016 Lisboa, Portugal
[e] BSIRG, iBB - Institute for Bioengineering and Biosciences, Associate Laboratory i4HB - Institute for Health and Bioeconomy, and Chemical Engineering Department at Instituto Superior Técnico, Universidade de Lisboa, 1049-001 Lisbon, Portugal
§ A.R.R share the first authorship with S. R.

Abstract: Continuous advancements in understanding and controlling surface functionalisation and properties empower materials scientists to design materials with tailored characteristics, improved performance, and enhanced functionality, thereby expanding scientific knowledge and technological progress. This research paper presents the synthesis of two new metal-organic material-based films using the cathodic electrodeposition method. In contrast with the anodic deposition method, the cathodic deposition method offers the advantage of using non-metal electrode substrates and various metal ions, a unique aspect not yet fully explored. The study investigates the effects of linker length using 2,5-dihydroxyterephthalic acid (**DOBDC**) and 3,3'-dihydroxybiphenyl-4,4'-dicarboxylic acid (**BPP**) as organic linkers and iron(III) as the metal node for the structures. The films' electrochemical behaviour, characterisation through techniques like infrared spectroscopy, scanning electron microscopy, X-ray photoelectron spectroscopy, X-Ray powder diffraction and grazing-Incidence small-angle X-ray scattering and particle-induced X-ray emission, as well as results from cyclic voltammetry studies, are discussed. The films were found to be nearly amorphous with specific grain sizes, revealing heterogeneity in composition and thickness. The unique synthesis method and comprehensive characterisation offer insights into the potential of electrosynthesis for designing functional materials and encourage further exploration of various synthesis conditions and metal ions.

Introduction

New functionalised surfaces are crucial for the development of materials science, as they enable the exploration of novel properties and functionalities, expand the range of applications for materials, and drive innovation in different industries. By continually advancing the understanding and control of surface properties, materials scientists can unlock new possibilities for designing materials with tailored characteristics, improved performance, and enhanced functionality, thereby pushing the boundaries of scientific knowledge and technological development.[1–3] The newly designed materials can have new or improved properties such as conductivity, reactivity, photoactivity, and catalytic performance.[2]

There are several physical and chemical methods for the formation of thin films based on inorganic and/or organic compounds such as atomic layer deposition, sputtering, chemical vapour deposition, metal-organic chemical vapour deposition, molecular beam epitaxy, electrodeposition, spin-coating, among others.[4] Many candidates have been used for deposition as metal oxides[5], nanoparticles[6,7], polymers,[8,9] metal alloys[10] and among them, metal-organic materials (MOMs) started to attract attention due to their outstanding film-forming properties, diverse metal centres and ligand sources,

and the ability to design both their structure and function.[11,12] MOMs are built from the self-assembly of metal ions (nodes) and organic ligands (linkers) and are exemplified by a vast group of discrete (e.g. metal–organic polyhedra, spheres or nanoballs, metal–organic polygons) or polymeric structures (e.g. porous coordination polymers, PCPs, metal–organic frameworks, MOFs, or hybrid inorganic–organic materials).[13] Presently, attention is broadening materials that are commonly identified as CPs[14] or MOFs[15], with the latter designation applying to structures that are crystalline and feature high porosity.

Although MOMs date back to the 1950s, interest in supramolecular metal–organic thin films is escalating due to their extensive selection of components, hybrid physicochemical characteristics, and adaptable reactivity.[1,16–20] Moreover, understanding the self-assembly mechanisms enables precise manipulation of the structural and functional features of the films.[21] Their structural and chemical versatility continues to fuel scientific intrigue and technological advancements, paving the way for customization in several applications from gas management and separation to advancements in sensing, catalysis, photonics, electronics, and energy solutions.[11,22]

Here we report the synthesis of two new MOM-based films using the cathodic electrodeposition method (Fig. 1a) that allows to have shorter synthesis times under milder conditions and the ability to fine-tune morphology as key advantages.[23] When compared with the anodic dissolution method, it gives the possibility of using non-metal electrode substrates and different metal ions. This method has not been yet explored for a wide range of metal ions and linkers, which gives a great opportunity to develop the state-of-the-art by solidly developing a transferable methodology for highly controlled synthesis of MOM films. Two distinct organic linkers (Fig. 1b) were selected to investigate the effect of the linker length, namely 2,5-dihydroxyterephthalic acid (**DOBDC**) and 3,3'-dihydroxybiphenyl-4,4'-dicarboxylic acid (**BPP**). $FeCl_3.6H_2O$ was used as the metal salt for providing iron as metal node for the MOM film, since upon electroreduction, a possible mixed-valence state could potentially boost the conductivity.[24] With this, it is reasonable to assert that an elevated understanding of the molecular processes at interfaces will enhance the knowledge of the research field to build new and improved functional interfaces.

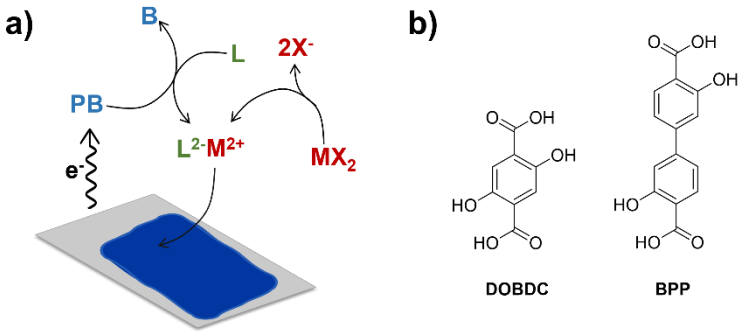

Fig. 1 a) Linkers used in this study. b) Mechanism of the cathodic deposition of MOMs (PB = Probase, B = Base, M = metal node, L = organic linker).

Results and discussion

Electrochemical studies for electrosynthesis optimisation.

Cyclic voltammetry (CV) studies (Fig. 2) on the precursors were performed to find the optimised potential to use for the potentiostatic growth of MOM films using two different linkers (Fig. 1b, **DOBDC** and **BPP**). The studies were performed in dimethylformamide (DMF) and using 0.1 M tetrabutylammonium hexafluorophosphate ($TBAPF_6$) as supporting electrolyte. Fluorine tin oxide

(FTO, a thin film of tin oxide-doped with fluorine on glass substrate), platinum wire and Ag/AgCl (3M NaCl) were used as working, counter and reference electrodes, respectively. Besides the metal ion source and the pro-ligand, a pro-base (**PB**) must be used for the cathodic electrodeposition to deprotonate the pro-ligand.[25] In contrast to other deposition methods, the electrosynthesis method operates without pressure or temperature, and without the need of an extra step for powder immobilisation. Additionally, it enables the direct electrode surface deposition of a thin film, whereas post-solvothermal MOM powder synthesis needs an extra step for thin film deposition.

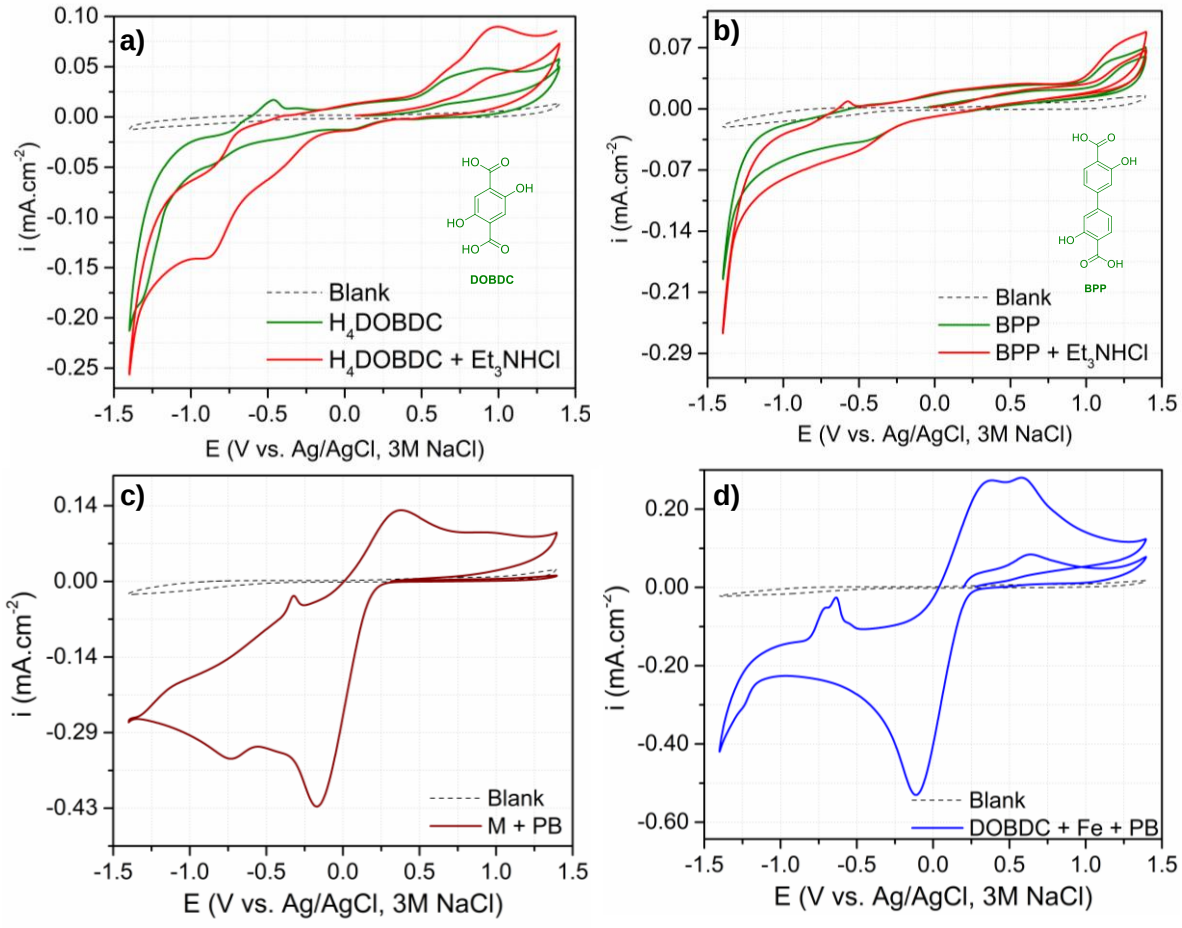

Fig. 2 Cyclic voltammograms of **DOBDC** a) and **BPP** b) (2 mM) with and without Et_3NHCl (2 mM). Cyclic voltammograms of a mixture of $FeCl_3.6H_2O$ (4 mM) and **PB** (2 mM) c) and after **DOBDC** (2 mM) is added d) in 0.1M TBAPF6 / DMF solutions under N_2 atmosphere at 100 mV s^{-1}. 0.1 M $TBAPF_6$ was used as supporting electrolyte. FTO (0.7 cm^2) was used as working, platinum wire as counter and Ag/AgCl (3M NaCl) as reference electrodes.

Et_3NHCl was used as **PB** to perform the deposition because its reductive potential is more positive than other more commonly used PBs (e.g. H_2O, NO_3^-, O_2) , preventing metal deposition.[26,27] CV (Fig. S1) of the **PB** shows its reduction to Et_3N and H_2 at around -0.6 V *vs.* Ag/AgCl (3 M NaCl) as reported in a 0.1 M $TBAPF_6$ DMF solution.[26,27] When **DOBDC** is added to the **PB** solution (Fig. 2a) a higher cathodic current density is observed as an increase in proton concentration is expected, as previously observed by Li *et al.*[27] A similar behaviour is observed when **BPP** is used (Fig. 2b).

A solution containing $FeCl_3.6H_2O$ (**M**) and **PB** (without the organic ligand) was also investigated (Fig. 2c) and the CV shows that the **PB** influences the iron redox behaviour (Fig. S2a), as the reduction of Fe(II) to Fe(0) (above -1.2 V, Fig. S2a) and the current density of its reoxidation to Fe(II) (-0.4 V, Fig. S2b) substantially decreases. Therefore, the presence of the **PB** may prevent the undesirable deposition of Fe(0) at the FTO. When all the precursors for the film formation are present in solution

(**M** + **PB** + **DOBDC** or **BPP**, Fig. 2d), the redox processes from the metal ion and the pro-ligands are observed with an additional oxidation process at 0.60 V, which was also present when only the metal source and the pro-ligand were mixed (Fig. S2b). In addition, the process from the reoxidation of Fe(0) is substantially reduced. The results suggest the formation of a complex between **M** and **DOBDC** that will be further discussed in detail.

Attempts to deposit thin films with these precursors onto FTO were performed by applying different potentials (-1.2, -1.3 and -1.4 V) to the 0.1 M $TBAPF_6$ DMF solutions containing **M**, **PB** and **DOBDC** or **BPP**. No deposition occurred when -1.2 V was applied to the electrolyte containing **DOBDC**, while it occurred when **DOBDC** was replaced by **BPP**. Therefore, -1.3 and -1.4 V were used for **DOBDC** and -1.2 and -1.3 V for **BPP** (Fig. S3-S4). The steady-state current density for the electrodeposition (Fig. S3-S4) reached values in the range of -90 to -220 μA cm^{-2} for all cases.

Infrared spectroscopy.

Under the cathodic deposition conditions discussed above, new films were formed on the FTO surface (Fig. 3 and S5) that were analysed by infrared spectroscopy (IR). Fig. 3 and S5a display the comparison between the IR spectra of the pro-ligands and the films grown at -1.3 V (**Film1** for **DOBDC** and **Film2** for **BPP**), and no significant difference was observed between the spectra of the films grown at the other potentials used for each case. The IR spectrum of **DOBDC** shows the typical bands at 3520 cm^{-1} ($\nu_{O\text{-}H,phenol}$), 3082 cm^{-1} ($\nu_{O\text{-}H,acid}$), 3024 cm^{-1} ($\nu_{C\text{-}H,aromatic}$), 1646 cm^{-1} ($\nu_{C=O}$), 1427 cm^{-1} ($\delta_{C\text{-}O,acid}$), 1357-1182 cm^{-1} ($\nu_{C\text{-}O,acid/phenol}$) and 782 cm^{-1} ($\delta_{C\text{-}H,Bz\ out\text{-}of\text{-}plane}$) cm^{-1}. For **Film1** as expected, the bands at 3520 cm^{-1} disappears and the band at 1646 cm^{-1} gives rise to the asymmetric and symmetric stretching bands of the carboxylate groups at 1538 cm^{-1} and 1417 cm^{-1}. Coordination of the iron centres is suggested in both phenolate and carboxylate groups of the **DOBDC** ligand. The same is observed for **BPP** and **Film2** (Fig. S5a).

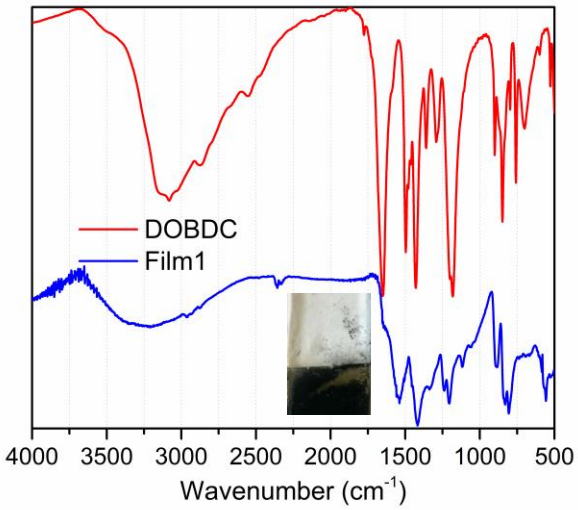

Fig. 3 IR spectra of **DOBDC** (red) and **Film1** (blue) formed by cathodic electrodeposition at -1.3 V *vs.* Ag/AgCl (3M NaCl). Inset: Picture of the film on the electrode.

Prior to film deposition, and after adding **DOBDC** to the DMF solution containing **M**, a colour change was observed. The IR spectrum of the solid residue of this solution is shown in Fig. S5b. The IR spectra of the residue and the film deposited are different (Fig. S5b). Although the stretching bands of carboxylate groups are observed (1575 cm^{-1} and 1413 cm^{-1}), the stretching band of the phenoxyl (3419 cm^{-1}) is also observed. The result indicates that deprotonation of the carboxylic acid groups occurs

immediately, whereas the phenoxyl is only deprotonated during cathodic electrodeposition. In fact, the results agree with previous reported studies, where the synthesis of MOF-74 proceeding through the generation of distinct phases is stated. In some cases the synthesis displays exclusively carboxylate coordination.[28–31]

Scanning electron microscopy.

The morphology of the films was observed by SEM (Fig. 4 and S6). For both **Film1** and **Film2**, islands of plate-like aggregates were imaged with a non-homogeneous dispersion. A plate-size of approx. 1 μm constitutes the aggregates in **Film1**, whereas smaller particles (< 1 μm) are observed for **Film2**. The distribution of the aggregates is different in both films, fewer empty areas are observed for **Film2**.A BET surface of approximately 1161 $m^2 g^{-1}$ was obtained for **Film1**.

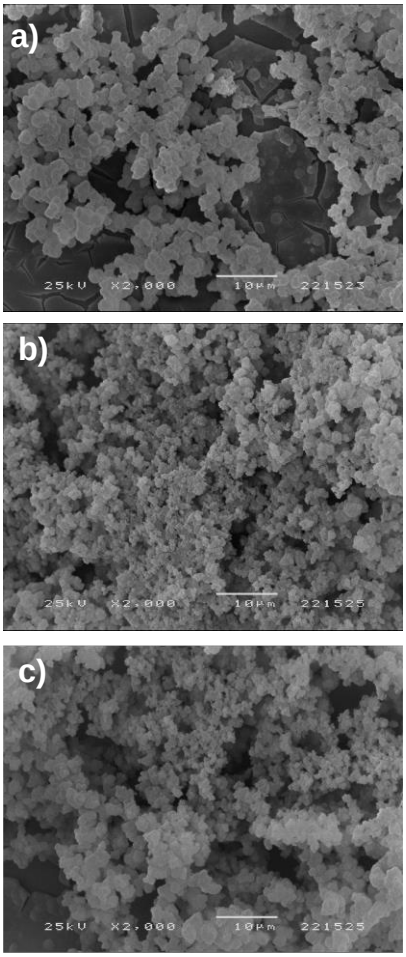

Fig. 4 SEM images (x 2000) of a) **Film1**, b) **Film2** and c) **Film1-T** after temperature treatment (100 °C for 12 h followed by 200 °C for 2 h).

X-Ray powder diffraction and grazing-Incidence small-angle X-ray scattering.

Both coatings, Film1 and Film2, are amorphous (or with very small grain sizes), as no X-ray diffraction (XRD) patterns was observed in the conventional Bragg-Brentano geometry. Even when a temperature treatment (100 °C for 12 h followed by 200 °C for 2 h)[32] labelled as **Film1-T** (Fig. 4c) was performed in **Film1**, no XRD pattern was observed. The lack of diffraction suggests a poor crystallisation process.

To explore the (lack of) crystallinity, grazing incidence small angle X-ray scattering measurements (GISAXS) were performed in the **Film1** and **Film2** and compared to the ones from the FTO and the glass substrates (Figs. 5 and 6). GISAXS, as a surface sensitive scattering technique, provides

information on the nano-scale volumes deposited on surfaces,[33] e.g., the crystallinity of the aggregates, observed in Fig. 4.

According to Figs. 5a and 5b, at the first glance, the two samples present similar GISAXS maps. Very similar maps were observed for the glass substrate and FTO (not shown). Using the mass density of Fe/C, a critical angle of 0.38 °/0.22 ° is determined whereas, from the critical angle, a maximum penetration depth of 6.7 nm/8.8 nm is deduced. For α<0.38 °, the penetration depth is lower than the expected for the thickness of **Film1** and **Film2** (few hundreds of nanometres). Thus, no effect due to the FTO is expected in the GISAXS measurements around the critical angle.

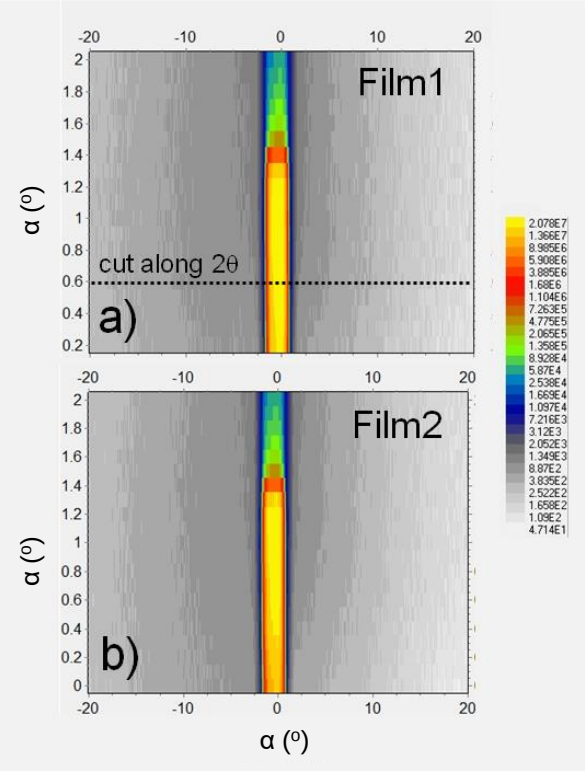

Fig. 5 Maps of the GISAXS measurements acquired for samples **Film1** (a), and **Film2** (b).

Fig. 6 compares the individual cuts along 2θ for each α of the GISAXS maps acquired for the FTO (a1-3), glass substrate (b1-3) and **Film1**/**Film2** (c/d1-3), respectively. Figures 6 a2), b2) and c2) correspond to the magnification along the intensity y-axis, while a3), b3) and c3) are plotted by considering the 2θ axis between -15° and 10 °. A broad peak-like structure is present in the negative 2θ for **Film1** and **Film2** while for the FTO and glass substrate, there is no clear diffraction. At the same time, **Film1** also exhibits a small peak for positive 2θ suggested to be due to the very small grain sizes. The full width at half maximum of the peaks observed for negative 2θ is highly inaccurate but can be estimated to be around 10° which, according to the Scherrer formula, can correspond to grain sizes of around 1 nm. The temperature treatment did not change the shape of the particles, however larger islands were formed with a higher quantity of aggregates (Fig. 4c).

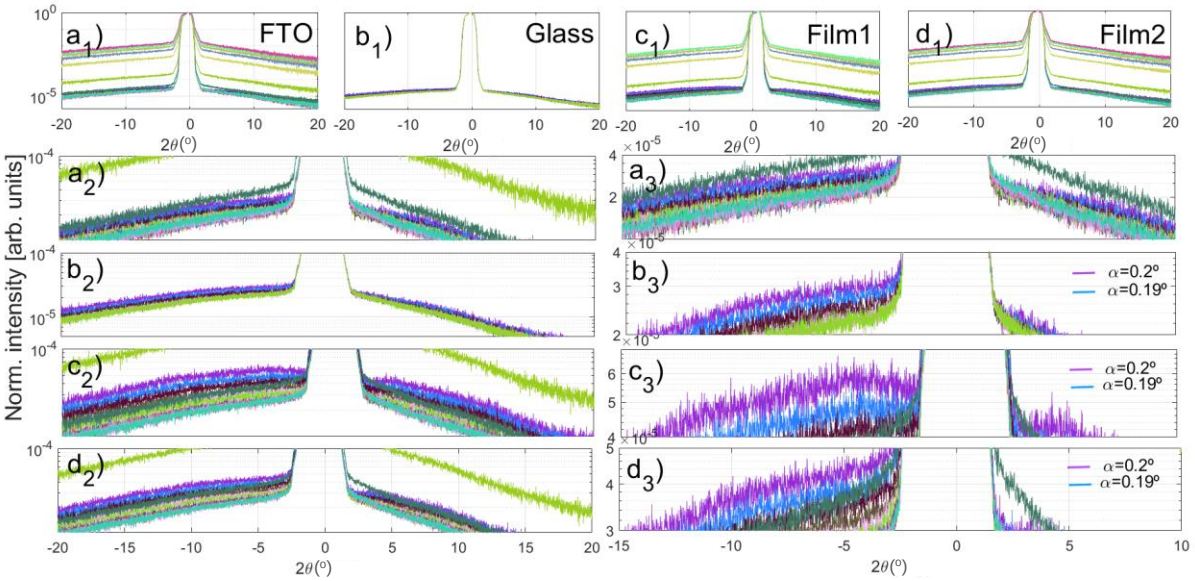

Fig. 6 Maps of the GISAXS measurements acquired for samples **Film1** a), and **Film2** b).

X-ray photoelectron spectroscopy.

The samples **Film1**, **Film2** and **Film1_-1.4V** were analysed by XPS. In addition, a film grown from a solution at -1.3 V without the pro-ligand was obtained (**FilmFe**) and analysed for comparison. In all the analysed samples, the elements carbon, iron, oxygen, nitrogen, chlorine and fluorine were detected. The detected fluorine has no counterpart of Sn in the major part of the samples; therefore, it is not assignable to the FTO substrate but rather to some electrolyte. The global quantification is gathered in Table S1.

The detailed regions for Fe 2p, O 1s and C 1s are shown in Fig. 7 and the corresponding data on fitted positions and atomic % are presented in Table S2.

C 1s region was fitted with three components: one set to 285 eV and used as reference for correction of binding energy shifts due to charge accumulation and assigned to carbon bonded to other carbon or hydrogen atoms; a second one ranging from 286.4 eV to 286.9 eV assigned to carbon bonded to oxygen through single bonds. For all the films, excepting **FilmFe** that is the one that was formed from a solution without the pro-ligand, this component is due to phenolic groups in the ligands.[34] A third component was fitted at 288.7±0.2 eV and assigned to carboxylate groups. Therefore, the ligands have the carboxylic group mainly deprotonated.[35] For the **FilmFe**, the detected carbon is entirely assignable to the presence of supporting electrolyte, pro-base or solvent.

O 1s regions present a component at 530.1±0.2 eV, assignable to the lattice oxygen in iron oxides, for **FilmFe** and **Film1_-1.4V**. It is not surprising that iron oxides are observed also for **Film1_-1.4V**, as a more reductive potential will lead to higher iron deposition.[26] In **FilmFe**, as expected, it is the main component. Besides, also a component centred at 531.3 eV assignable, mainly, to Fe-O-H groups is detected at the surface. The binding energies of **Film1** and **Film2** were fitted with two components at 531.6±0.2 eV assignable to the two equivalent oxygen atoms in the carboxylate group (O=C-O–) and another at 532.5±0.2 eV assigned to deprotonated phenolic oxygen, respectively (for protonated phenolic oxygen, O1s binding energy should be 533.5 eV).[34] The same was obtained for **Film1_-1.4V** spectrum, besides the above referred peak at ~530 eV. Moreover, qualitatively, the shape of the iron region of these films is very similar to the shape found for **FilmFe** strongly suggesting that the oxidation state of iron in the complexes is Fe(III).

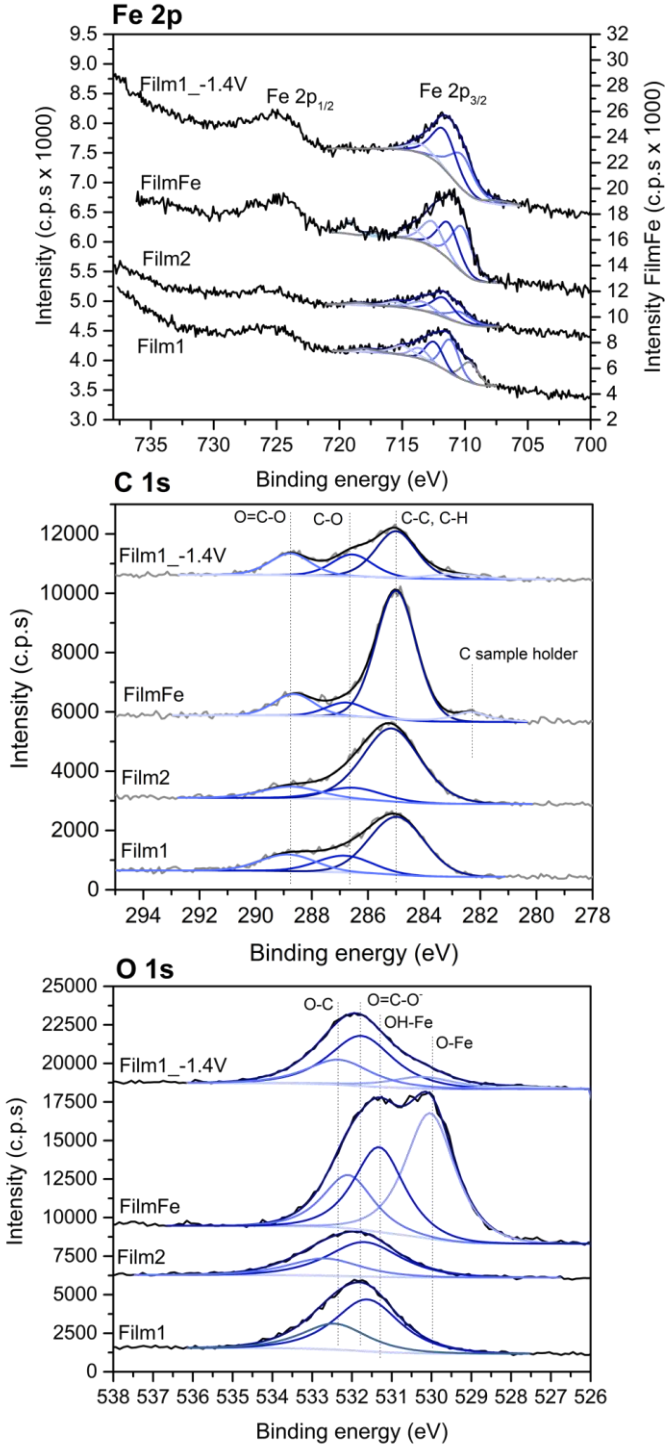

Fig. 7 XPS regions Fe 2p, C 1s and O 1s for **Film1**, **Film2**, **FilmFe** (all three films were deposited at -1.3 V) and **Film1_-1.4V**, from bottom to top.

Particle-induced X-ray emission and Rutherford backscattering spectrometry.

As the films are heterogeneous, PIXE and RBS techniques were employed simultaneously to characterise the surface and to obtain in-depth chemical information for both **Film1** and **Film2**. As the films are heterogeneous, we decided to perform a surface and an in-depth characterisation of both **Film1** and **Film2** using simultaneously PIXE and RBS techniques. 2D elemental distribution maps of Fe and Cl were obtained from the PIXE spectra and the Sn map from RBS spectra (Fig. 8 and S7). From

the distribution maps the films' surface heterogeneity is again revealed (cf. with SEM images). Also, while the Fe and Cl distributions are correlated, the Sn map (from the FTO electrode) shows an opposite correlation, with higher Sn signal in the low film thickness zones indicating irregular film coverage with different thicknesses. Similar behaviour was registered for **Film2** with different degree of coverage. Point analyses (Fig. 8, red circles in the maps) allowed to know the inorganic composition of the films from the PIXE spectra analysis, where only Fe, Cl and P were detected as film constituents (Si, Ca and Sn were also detected but attributed to the glass substrate and FTO layer).
For **Film1**, concentration values of Fe, Cl and P in different points of the film (Fig. 8) were 90 wt.%, 3wt.% and 5 wt.% respectively, while for **Film2** slightly different values were recorded, 88-89 wt.% for Fe, 10 wt.% for Cl and less than <1 wt.% for P. Besides the composition of the films, it was possible to estimate their thickness on the different points analysed from the RBS spectra. While for Film1 the thickness values obtained are higher than 10 μm, the thickness of **Film2** varies between 1.4 and 2.5 μm (Fig. S7), allowing also to detect the presence of FTO and the glass substrate. An example of a PIXE and RBS spectra from **Film2** are shown in Fig S8.

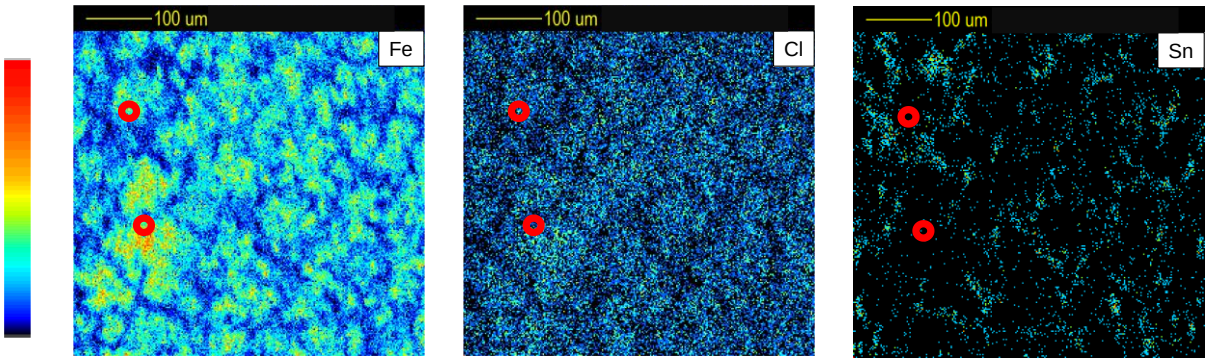

Fig. 8 Fe, Cl and Sn 2D elemental distribution of **Film1** (grown at -1.3 V) obtained by PIXE and RBS spectra (circles indicate location of the analyses performed).

From the fit of the RBS spectra recorded in different points of the films it was possible to obtain a depth profile for **Film1** and **Film2** (Fig. 9). In both cases, it is possible to observe that there is more than one region where the same atom is found at a different concentration, highlighting the in-depth heterogeneity of these films. For **Film2**, it was possible to analyse all the in-depth profile until reaching the FTO layer and the glass, whereas this was not possible for **Film1** as it is much thicker than **Film2**. Moreover, the amount of Fe in **Film1** generally decreases in-depth, which is suggestive of a pre-layer of iron oxides/hydroxides. The same was not observed for **Film2**. In fact, the different between the concentration of iron at the surface for **Film2** is almost zero. To clarify if there is deposition of the pro-ligand at the electrode surface, a solution without the **M** was used for an attempt of deposition using the same conditions previously used for **Film2** – no film was obtained. In tables S3 and S4 are shown the Fe/O and Fe/C ratios for both films.

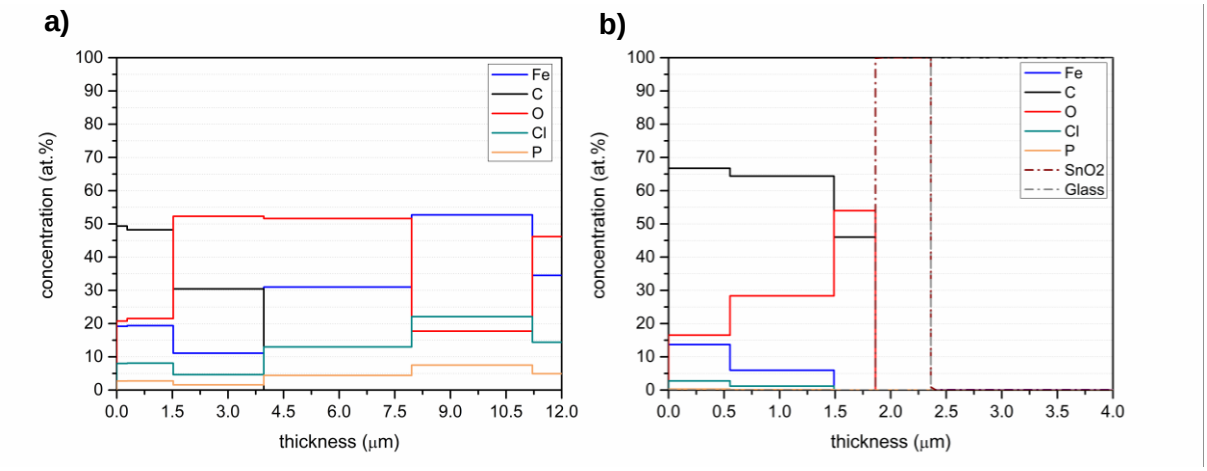

Fig. 9 Elemental depth profile of a) **Film1** and b) **Film2** (both films grown at -1.3 V).

Atomic force microscopy – analysing growth with deposition time

The morphology of **Film1** was studied over different deposition times to conclude about the film organisation and morphology along the different deposition stages. These were deposited with a growth potential of -1.3 V *vs.* Ag/AgCl (3M NaCl) with deposition times ranging from 8 seconds to 45 minutes, over FTO substrates (Fig. S9).

The FTO electrode (Fig. S10), as well as the films deposited for 8 and 20 seconds and 15, 20 and 30 minutes were characterised by AFM, obtaining both 2D and 3D images (Fig. S11-S15). Although AFM did not characterise the films crystallinity, it revealed morphological information, as well as approximate values of film depth. The AFM images of FTO showed a rough material, with a morphology characteristic of metal oxides. The images of the 8- and 20-second films show a very ordered morphology, with a dune-like consistency at 8 seconds, that formed terraces at 20 seconds (Fig. 10). The morphologies of the 15-, 20- and 30-minute films agree with the SEM images of the 1-hour films. Herein, it was also noted that the films were constituted by disc-shaped aggregates stacked on top of each other. Moreover, the AFM image of the 30-minute film presents a different layer depositing on top of the stacked aggregates, which could be due to an unorganised growth. This new layer could be further analysed by the 45-minute or 1-hour films, however, they were too thick to be characterised by AFM.

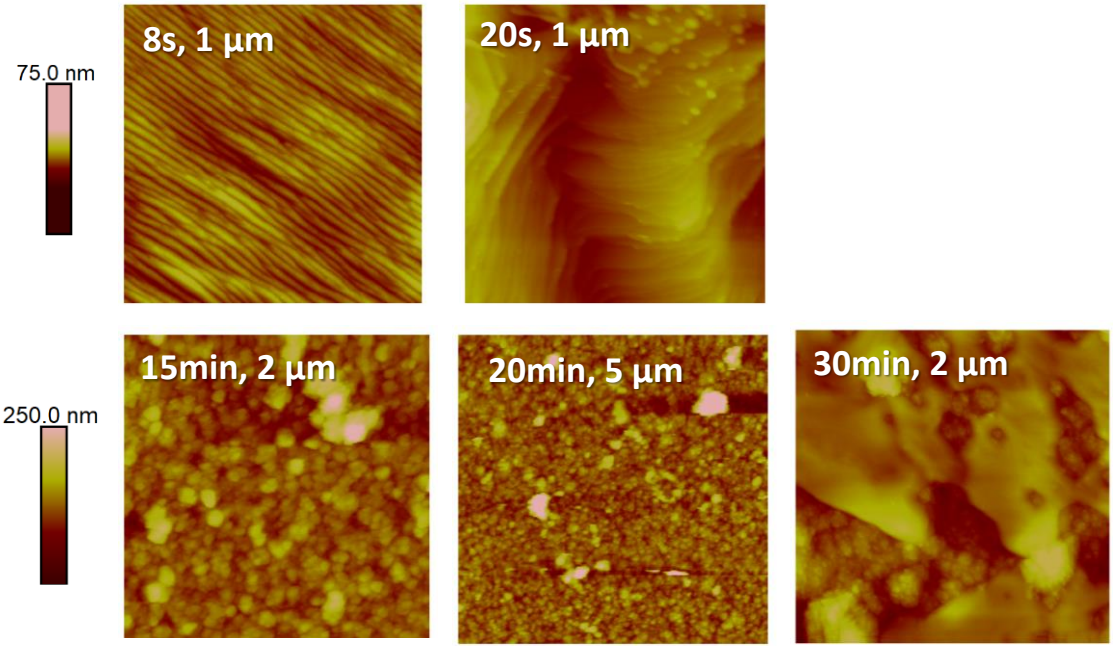

Fig. 10. 2D AFM images of deposited Film1 (2:1:1 ratio of **M:DOBDC:PB**, respectively) deposited for 8 and 20 seconds (1 x 1 µm) and 15, 20 and 30 minutes (2 x 2 µm).

The approximate thickness of the 8- and 20-second films was obtained by taking cross sections on topographical images, reaching values of at least 15 nm and 185 nm, respectively (Fig. S16). These shorter deposition approaches could be advantageous if the films were proven to be crystalline by XRD. On the other hand, this fast rate could be associated with a random growth and be one of the causes of obtaining an amorphous **Film1** film. For comparison, the **FilmFe** was also analysed by AFM (Fig. S17). The images showed a typical metal oxide morphology, similar to FTO, as already expected. This agrees with the presence of an iron oxide/hydroxide film.

Electrochemical and voltametric behaviour.

The new films formed are electrochemically active due to the presence of iron metal centres. Therefore, their electrochemical behaviour was investigated in a DMF solution. For **Film1**, one pair of redox waves (E_p^{ox} = -0.16 V and E_p^{red} = -0.34 V) is detected and may be attributed to the Fe^{3+}/Fe^{2+} couple. Similar redox processes are observed for **Film2** (Fig. 11). In addition, the films are stable, as no current loss is observed after several cycles. The oxidation and reduction peak currents were plotted as a function of the scan rate for Film1 (Fig. S18) and the proportional relationship shows that the electrode processes are adsorption-controlled. However, when the same graphs were plotted for **Film2**, the reduction peak current density does not show a proportional relationship (Fig. S19a and S19b). As no loss of material from the electrode surface is observed by performing several potential cycles with the film (Fig. 11), the absence of a proportional relationship is attributed to electron-transfer constraints within the film. However, when the film is grown at a lower potential (-1.2 V) a linear relationship is observed (Fig. S19c and S19d) showing adsorption-controlled processes without the constraints previously discussed. Therefore, the linker affects the film properties. We can state that the linker affects the film properties.

The electroactive surface coverage (Γ_e, nmol cm^{-2}) was estimated for both **Film1** and **Film2** based on the integrated charges of the Fe^{3+}/Fe^{2+} redox process and the values obtained were 7.8 for **Film1** and 2.2 for **Film2**.

The voltammetric behaviour using ferrocene as a probe of the films was also investigated and a linear relationship between peak currents and the square root of the scan rate, $v^{1/2}$, confirms a diffusion-

controlled process for **Film1** and **Film2** (Fig. S20). As the films are not dense and the FTO is also exposed, the FTO (Fig. S20) voltammetric behaviour was investigated and compared with the films. It is possible to observe that the voltammetric response exhibited by both films can be attributed to the exposed FTO surface. In the case of the less dense **Film1**, the redox behaviour of Ferrocene closely resembles that of the FTO surface, whereas **Film2**, which is denser (as evident in SEM images), results in a reduced current observed during the Ferrocene redox processes.

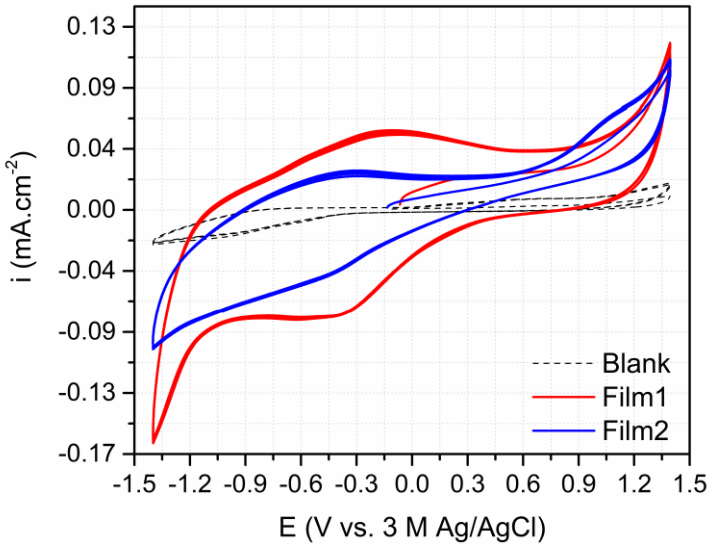

Fig. 11 Redox behaviour of **Film1** and **Film2** (electrodeposited at -1.3 V) in DMF solutions at 100 mV s^{-1}. 0.1 M $TBAPF_6$ was used as supporting electrolyte. FTO (0.7 cm^2) was used as working, platinum wire as counter and 3 M Ag/AgCl as reference electrodes. 6 cycles.

Conclusions

New iron-organic based films with two organic pro-ligands with different lengths were prepared. To prepare the films, we used the cathodic deposition method which is a milder and a fine-tuneable method when compared with other synthesis methods. CV studies were performed to optimise the deposition conditions, namely, the potential used to potentiostatically grow the films (range between -1.2 V and -1.4 V, depending on the pro-ligand). In addition, when a more negative potential is applied a pre-layer of iron oxide/hydroxide is formed, supported by XPS analysis. Using IR, mixing the pro-ligand and the metal source in a DMF solution, a compound where the carboxylate is coordinated to the iron centre is obtained. However, the phenol group is only deprotonated after the cathodic electrodeposition procedure yielding an amorphous film. Both films are found to be nearly-amorphous with a grain size of about 1 nm as found via GISAXS measurements. SEM images show plate-like aggregates with a non-homogeneous dispersion. XPS analysis confirmed the composition of the films and the deprotonation of both phenol group and carboxylic group. The in-depth characterisation of the films combining PIXE and RBS showed that both films are very heterogenous and that different pro-ligands yield films with very different thicknesses. The expected atoms (namely, Fe, O, C) were identified and different concentrations were found along the films thickness with no iron pre/layer formed when the film is grown at -1.3 V using **BPP** (**Film2**). The electrochemical behaviour of the films showed high stability upon six cycles in DMF solution. After the analysis of the redox processes of both films with the scan rate, a difference is obtained when the pro-ligand has a higher length. **Film1** showed a good voltammetric behaviour when exposed to a solution with a probe (ferrocene).

Although nearly amorphous films were obtained, this study clearly opens a way to investigate different electrosynthesis conditions (e.g.: metal ion, deposition time, solvent).
Attempts with other metal ions are ongoing.

Materials and methods

General procedures.
If not stated otherwise, all chemicals were used without further purification and purchased from TCI, Sigma Aldrich, Fluorochem and Acros Organics. BPP was synthesised according to the literature.[36] When indicated, solvents were purified as described by Amarin and Perrin.[37]
^{1}H and ^{13}C NMR spectra were recorded on a Bruker Advance 400 MHz spectrometer. Powder IR spectra were obtained on a Nicolet Nexus 6700 FTIR spectrophotometer in the 400-4000 cm^{-1} range with 4 cm^{-1} resolution using KBr pellets with 64 scans. Film DR-FTIR spectra were obtained with the same spectrophotometer with the DR (diffuse reflectance) accessory in the 600-4000 cm^{-1} range with 4 cm^{-1} resolution and 256 scans.

Electrochemical experiments. Generally, a potentiostat PGSTAT 12 AUT71019 controlled by NOVA 2.0 software was used. For all the experiences, a three-electrode electrochemical heart-shaped glass cell was used. As for the electrodes, a platinum wire as a counter electrode and Ag/AgCl, 3M NaCl (0.278 V *vs.* NHE) as a reference electrode. The working electrode was a FTO electrode with 0.7 cm^2. FTO electrodes were ultrasonically washed before experiments with a detergent/water solution, methanol, and acetone for 15 min with each solution. Before any electrochemical measurements, the cell solutions were purged by bubbling N_2 for a minimum of 30 minutes. 0.1 M of $TBAPF_6$ was used as the supporting electrolyte, which was previously recrystallised from hot ethanol.
Both cyclic voltammetry and chronoamperometry experiments were performed under an organic medium with 10 mL of DMF with 0.1 M of $TBAPF_6$ with or without other components. For the deposition on the films, the precursor solution was constituted by the metal ion (**M** = $FeCl_3.6H_2O$), the pro-ligand (**DOBDC** or **BPP**) and the pro-base (**PB** = Et_3NHCl) in a ratio of 2:1:1 (**M:PL**:**PB**, respectively). One-step electrodeposition was performed by applying -1.4, -1.3 or -1.2 V *vs.* reference electrode for 1h. After the deposition, the electrode was dried at room temperature and washed with DMF and acetone.
The films were studied for their redox and voltametric behaviour in DMF solution containing 0.1 M $TBAPF_6$ with or without 1 mM of ferrocene.

Physical characterisations. SEM images were obtained by means of a JEOL JSM-5200LV scanning electron microscope. Previously, the films were mounted in stubs and coated with gold in a JEOL JFC-1200 sputtering chamber.
Diffractograms were acquired using a Philips Analytical PW 3050/60 X'Pert PRO automatic diffractometer (θ/2θ), equipped with an X'Celerator detector, with automatic data acquisition using the X'Pert Data Collector software, version 2.0b. As incident radiation, the Kα line of a copper bulb was used, operating with a current of 30 mA and a voltage of 40 kV. To record the diffractograms, a continuous scan of the Bragg angles was performed, for values of 2θ, between 10° and 90°, with a step of 0.017° (2θ) and an acquisition time of 20 s/step. The GISAXS spectra were acquired using a Bruker D8 AXS diffractometer equipped with a Cu source. To limit the vertical divergence, a Göbel mirror and a Söller slit were used in the primary and secondary beam paths, respectively. The measurements were performed with a 2θ step of 0.01° ranging from -20° to 20° and a α step of 1° from 0° to 2°. The accumulation time is set to 1 s/step. The system operated at 40 mA / 40 kV. The

diffracted/reflected counts per second were registered in a proprietary software (Commander) using a point focus detector.

For PIXE and RBS techniques it was used a 2MeV proton beam generated by a 2.5 MV single ended Van de Graaff accelerator and directed to the microprobe beam line through a 90° bending magnet. The nuclear microprobe has an Oxford Microbeams magnetic quadrupole triplet used to focus the beam up to 3x4 μm^2.[38] The measurements are performed under vacuum conditions and the experimental chamber has a 30 mm^2 Bruker Si SDD detector with 8 μm Be window and 145 eV resolution at 5.9 keV, positioned at 135° with the beam direction at a distance of 20 mm from the sample, used to record the PIXE spectra. The backscattered protons are detected with a 200 mm^2 PIPS detector with 30 keV resolution, positioned at 140° scattering angle in Cornell geometry at a 50 mm distance from the sample. Operation and basic data manipulation, this including elemental distribution mapping, was achieved through the OMDAQ software code. Quantitative PIXE spectra analysis are done with GUPIX software[39] and the results are expressed in weight percent normalised to 100%. Furthermore, NDF v9.6a code simultaneously fits the PIXE and RBS spectra to obtain a self-consistent solution.[40] Thickness values are obtained in areal density (i.e., atoms/cm^2), the standard units in IBA analyses and they were converted into nm units considering the areal density and molecular mass of the compounds. The RBS fits considerer the double scattering contribution and the pulse pile-up effect. The non-Rutherford cross sections for C, O and Si were included in the fitting model[41], as well as the roughness of the surface using the Gamma roughness algorithm[42].

XPS analyses were performed with a dual anode (Al/Mg) non-monochromatic spectrometer XSAM800 from KRATOS. The X-radiation Mg Kα (hν = 1253.6 eV) used to irradiate the samples, was produced with a high voltage of 12 kV and filaments current equal to 10 mA. Samples were fixed to the XPS holder with a metal spring and positioned in the analysis chamber at a take-off angle of 90° relative to the surface. The analysis, at room temperature, started once the chamber attained an ultra-high vacuum (UHV), typically a pressure ~10-9 mbar. Spectra were acquired in a Fixed Analyser Transmission (FAT) mode, with a pass energy of 20 eV, and collected and stored in 300 to 400 channels with a step of 0.1 eV using the software Vision 2 for Windows, Version 2.2.9 (Kratos). No flood gun was used to compensate the charge accumulation. Charge shift was corrected from the spectra using as reference the binding energy (BE) of aliphatic carbon bonded to carbon and/or hydrogen, set at 285 eV. Source satellites and Shirley backgrounds were subtracted at each region of interest. Component peaks with pseudo-Voigt profiles were fitted in each region with a nonlinear least-squares algorithm using the XPSPeak 4.1 software (freeware), which allows to optimize simultaneously peaks position, area, full width at half maximum and Gaussian-Lorentzian %. The only constraints imposed were i) for all the components, within a given region, identical full width at half maximum (FWHM) and identical Lorentzian percentage; ii) for the peaks corresponding to carbon bonded to oxygen atoms (second and third components), identical areas. The sensitivity factors used in the quantification were the following: C 1s: 0.318; O 1s: 0.736; N 1s: 0.505; Fe 2p3/2: 1.965; Cl 2p: 0.964; P 2p: 0.530; P 2s: 0.344; F 1s: 1.000; Sn 3d5/2: 4.946; Na 1s: 1.378.

Acknowledgements

Centro de Química Estrutural (CQE), Institute of Molecular Sciences (IMS), iBB and i4HB acknowledge the financial support of Fundação para a Ciência e Tecnologia (Projects UIDB/00100/2020, UIDP/00100/2020, LA/P/0056/2020, UIDB/04565/2020, UIDP/04565/2020 and LA/P/0140/2020, respectively). The NMR spectrometers are part of the National NMR Network (PTNMR) and are partially supported by Infrastructure Project Nº 022161 (co-financed by FEDER through COMPETE 2020, POCI and PORL and FCT through PIDDAC).

S.R. and P.N.M acknowledge FCT for financial support (2020.02134.CEECIND and CEECIND/00509/2017). V.C. and L. C.A. acknowledge FCT for UIDB/04349/2020 project.

Keywords: Metal-organic materials; Cathodic electrodeposition; surface functionalisation; electrosynthesis; film characterisation

References

(1) Ma, T.; Zhang, J.; Zhang, L.; Zhang, Q.; Xu, X.; Xiong, Y.; Ying, Y.; Fu, Y. Recent Advances in Determination Applications of Emerging Films Based on Nanomaterials. *Adv. Colloid Interface Sci.* **2023**, *311*, 102828. https://doi.org/10.1016/J.CIS.2022.102828.

(2) Jiang, P.; Ji, Z.; Wang, X.; Zhou, F. Surface Functionalization-a New Functional Dimension Added to 3D Printing. *J. Mater. Chem. C* **2020**, *8*, 12380. https://doi.org/10.1039/d0tc02850a.

(3) Ruzybayev, I.; Ceylan, A.; Rumaiz, A. K.; Shah, S. I. *Thin Films, Film Formation Techniques*; John Wiley & Sons, Ltd, 2020. https://doi.org/10.1002/0471238961.0609121313012020.A01.

(4) Martin, P. M. *Handbook of Deposition Technologies for Films and Coatings*; 2010.

(5) Glynn, C.; O'Dwyer, C. Solution Processable Metal Oxide Thin Film Deposition and Material Growth for Electronic and Photonic Devices. *Adv. Mater. Interfaces* **2017**, *4* (2), 1600610. https://doi.org/10.1002/ADMI.201600610.

(6) Ahmed, S. R.; Kim, J.; Tran, V. T.; Suzuki, T.; Neethirajan, S.; Lee, J.; Park, E. Y. In Situ Self-Assembly of Gold Nanoparticles on Hydrophilic and Hydrophobic Substrates for Influenza Virus-Sensing Platform. *Sci. Reports 2017 71* **2017**, *7* (1), 1–11. https://doi.org/10.1038/srep44495.

(7) Gaviria, J.; Alcudia, A.; Begines, B.; Beltrán, A. M.; Villarraga, J.; Moriche, R.; Rodríguez-Ortiz, J. A.; Torres, Y. Synthesis and Deposition of Silver Nanoparticles on Porous Titanium Substrates for Biomedical Applications. *Surf. Coatings Technol.* **2021**, *406*, 126667. https://doi.org/10.1016/J.SURFCOAT.2020.126667.

(8) Žigon, J.; Kariž, M.; Pavlič, M. Surface Finishing of 3D-Printed Polymers with Selected Coatings. *Polymers (Basel).* **2020**, *12* (12), 2797. https://doi.org/10.3390/POLYM12122797.

(9) Noh, J.; Jeong, S.; Lee, J. Y. Ultrafast Formation of Air-Processable and High-Quality Polymer Films on an Aqueous Substrate. *Nat. Commun.* **2016**, *7* (1), 1–9. https://doi.org/10.1038/ncomms12374.

(10) Guo, Y.; Zou, Y.; Cheng, C.; Wang, L.; Made, R. I.; Goei, R.; Tan, K. W.; Li, S.; Tok, A. I. Y. Noble Metal Alloy Thin Films by Atomic Layer Deposition and Rapid Joule Heating. *Sci. Rep.* **2022**, *12* (1), 1–9. https://doi.org/10.1038/s41598-022-06595-9.

(11) Zhang, Y.; Chang, C. H. Metal-Organic Framework Thin Films: Fabrication, Modification, and Patterning. *Processes*. MDPI AG March 1, 2020, p 377. https://doi.org/10.3390/PR8030377.

(12) Zhang, Z.; Liu, C.; Zhang, H.; Xu, Z. K.; Ju, F.; Yu, C.; Xu, Y. Ultrafast Interfacial Self-Assembly toward Supramolecular Metal-Organic Films for Water Desalination. *Adv. Sci.* **2022**, *9* (24). https://doi.org/10.1002/ADVS.202201624.

(13) Perry, J. J.; Perman, J. A.; Zaworotko, M. J. Design and Synthesis of Metal–Organic Frameworks Using Metal–Organic Polyhedra as Supermolecular Building Blocks. *Chem. Soc. Rev.* **2009**, *38* (5), 1400–1417. https://doi.org/10.1039/B807086P.

(14) Kitagawa, S.; Kondo, M. Functional Micropore Chemistry of Crystalline Metal Complex-Assembled Compounds. *Bull. Chem. Soc. Jpn.* **1998**, *71* (8), 1739–1753. https://doi.org/10.1246/BCSJ.71.1739.

(15) Yaghi, O. M.; Li, H. Hydrothermal Synthesis of a Metal-Organic Framework Containing Large Rectangular Channels. *J. Am. Chem. Soc.* **1995**, *117* (41), 10401–10402. https://doi.org/10.1021/JA00146A033/SUPPL_FILE/JA10401.PDF.

(16) Rayner, J. H.; Powell, H. M. 67. Structure of Molecular Compounds. Part X. Crystal Structure of the Compound of Benzene with an Ammonia–Nickel Cyanide Complex. *J. Chem. Soc.* **1952**, No. 0, 319–328. https://doi.org/10.1039/JR9520000319.

(17) Ariga, K.; Leong, D. T.; Mori, T. Nanoarchitectonics for Hybrid and Related Materials for Bio-Oriented Applications. *Adv. Funct. Mater.* **2018**, *28* (27), 1702905. https://doi.org/10.1002/ADFM.201702905.

(18) Rubio-Giménez, V.; Galbiati, M.; Castells-Gil, J.; Almora-Barrios, N.; Navarro-Sánchez, J.; Escorcia-Ariza, G.; Mattera, M.; Arnold, T.; Rawle, J.; Tatay, S.; Coronado, E.; Martí-Gastaldo, C. Bottom-Up Fabrication of Semiconductive Metal–Organic Framework Ultrathin Films. *Adv. Mater.* **2018**, *30* (10), 1704291. https://doi.org/10.1002/ADMA.201704291.

(19) Komiyama, M.; Yoshimoto, K.; Sisido, M.; Ariga, K. Chemistry Can Make Strict and Fuzzy Controls for Bio-Systems: DNA Nanoarchitectonics and Cell-Macromolecular Nanoarchitectonics. *Bull. Chem. Soc. Jpn.* **2017**, *90* (9), 967–1004. https://doi.org/10.1246/BCSJ.20170156.

(20) Sakamoto, R. Bottom-up Creation of Functional Low-Dimensional Materials Based on Metal Complexes. *Bull. Chem. Soc. Jpn.* **2017**, *90* (3), 272–278. https://doi.org/10.1246/BCSJ.20160304.

(21) Li, Z.-Y.; Dai, J.-W.; Damjanovic, M.; akuya Shiga, T.; Wang, J.-H.; Zhao, J.; Oshio, H.; asahiro Yamashita, M.; Bu, X.-H.; Li, Z. Y.; Wang, J. H.; Zhao, J.; Bu, X. H.; Yamashita, M.; Dai, D. W.; Damjanovic, D.; higa, D. S.; Oshio, H. Structure Switching and Modulation of the Magnetic Properties in Diarylethene-Bridged Metallosupramolecular Compounds by Controlled Coordination-Driven Self-Assembly. *Angew. Chemie Int. Ed.* **2019**, *58* (13), 4339–4344. https://doi.org/10.1002/ANIE.201900789.

(22) Dzhardimalieva, G. I.; Uflyand, I. E. Design and Synthesis of Coordination Polymers with Chelated Units and Their Application in Nanomaterials Science. *RSC Adv.* **2017**, *7* (67), 42242–42288. https://doi.org/10.1039/C7RA05302A.

(23) Al-Kutubi, H.; Gascon, J.; Sudhölter, E. J. R.; Rassaei, L. Electrosynthesis of Metal-Organic Frameworks: Challenges and Opportunities. *ChemElectroChem* **2015**, *2* (4), 462–474. https://doi.org/10.1002/celc.201402429.

(24) Sun, L.; Hendon, C. H.; Park, S. S.; Tulchinsky, Y.; Wan, R.; Wang, F.; Walsh, A.; Dincă, M. Is Iron Unique in Promoting Electrical Conductivity in MOFs? *Chem. Sci.* **2017**, *8* (6), 4450–4457. https://doi.org/10.1039/c7sc00647k.
(25) Li, M.; Dincă, M. Reductive Electrosynthesis of Crystalline Metal-Organic Frameworks. *J. Am. Chem. Soc.* **2011**, *133* (33), 12926–12929. https://doi.org/10.1021/ja2041546.
(26) Zhang, B.; Huang, P.; Chen, J.; Dang, X.; Hu, Y.; Ai, Y.; Zheng, D.; Chen, H. One-Step Controlled Electrodeposition of Iron-Based Binary Metal Organic Nanocomposite. *Appl. Surf. Sci.* **2020**, *504*, 144504. https://doi.org/10.1016/J.APSUSC.2019.144504.
(27) Li, M.; Dincă, M. Selective Formation of Biphasic Thin Films of Metal–Organic Frameworks by Potential-Controlled Cathodic Electrodeposition. *Chem. Sci.* **2013**, *5* (1), 107–111. https://doi.org/10.1039/C3SC51815A.
(28) Rosnes, M. H.; Mathieson, J. S.; Törnroos, K. W.; Johnsen, R. E.; Cronin, L.; Dietzel, P. D. C. Electrospray Mass Spectrometry Investigation into the Formation of CPO-27. *Cryst. Growth Des.* **2019**, *19* (4), 2089–2096. https://doi.org/10.1021/ACS.CGD.8B01657/ASSET/IMAGES/LARGE/CG-2018-016576_0004.JPEG.
(29) Cheansirisomboon, A.; Salinas-Uber, J.; Massera, C.; Roubeau, O.; Youngme, S.; Gamez, P. One-Pot Multiple Metal–Organic Framework Formation: Concomitant Generation of Structural Isomers or of Drastically Distinct Materials. *Eur. J. Inorg. Chem.* **2014**, *2014* (26), 4385–4393. https://doi.org/10.1002/EJIC.201402475.
(30) Anderson, S. L.; Gładysiak, A.; Boyd, P. G.; Ireland, C. P.; Miéville, P.; Tiana, D.; Vlaisavljevich, B.; Schouwink, P.; Van Beek, W.; Gagnon, K. J.; Smit, B.; Stylianou, K. C. Formation Pathways of Metal–Organic Frameworks Proceeding through Partial Dissolution of the Metastable Phase. *CrystEngComm* **2017**, *19* (25), 3407–3413. https://doi.org/10.1039/C7CE00589J.
(31) Du Bois, D. R.; Wright, K. R.; Bellas, M. K.; Wiesner, N.; Matzger, A. J. Linker Deprotonation and Structural Evolution on the Pathway to MOF-74. *Inorg. Chem.* **2022**, *61* (11), 4550–4554. https://doi.org/10.1021/ACS.INORGCHEM.1C03988/ASSET/IMAGES/LARGE/IC1C03988_0004.JPEG.
(32) Garzón, L.; Garzón-Tovar, G.; Carné, A.; Carné-S ´ Anchez, C.; Carbonell, C.; Imaz, I.; Maspoch, D. Optimised Room Temperature, Water-Based Synthesis of CPO-27-M Metal-Organic Frameworks with High Space-Time Yields †. *J. Mater. Chem. A* **2015**, *3*, 20819. https://doi.org/10.1039/c5ta04923g.
(33) Levine, J. R.; Cohen, J. B.; Chung, Y. W.; Georgopoulos, P. Grazing-Incidence Small-Angle X-Ray Scattering: New Tool for Studying Thin Film Growth. *J. Appl. Crystallogr.* **1989**, *22* (6), 528–532. https://doi.org/10.1107/s002188988900717x.
(34) Beamson, G.; Briggs, D. *High Resolution XPS of Organic Polymers, the Scienta ESCA300 Database*; Wiley, Chichester, 1992.
(35) Pletincx, S.; Trotochaud, L.; Fockaert, L. L.; Mol, J. M. C.; Head, A. R.; Karslloğlu, O.; Bluhm, H.; Terryn, H.; Hauffman, T. In Situ Characterization of the Initial Effect of Water on Molecular Interactions at the Interface of Organic/Inorganic Hybrid Systems. *Sci. Rep.* **2017**, *7* (1), 1–8. https://doi.org/10.1038/srep45123.
(36) Grunder, S.; Valente, C.; Whalley, A. C.; Sampath, S.; Portmann, J.; Botros, Y. Y.; Stoddart, J. F. Molecular Gauge Blocks for Building on the Nanoscale. *Chem. - A Eur. J.* **2012**, *18* (49), 15632–15649. https://doi.org/10.1002/CHEM.201201985.
(37) Armarego, W. L. F.; Perrin, D. D. *Purification of Laboratory Chemicals*; Butterworth Heinemann, 1997.
(38) Alves, L. C.; Breese, M. B. H.; Alves, E.; Paúl, A.; Da Silva, M. R.; Da Silva, M. F.; Soares, J. C. Micron-Scale Analysis of SiC/SiCf Composites Using the New Lisbon Nuclear Microprobe. *Nucl. Instruments Methods Phys. Res. Sect. B Beam Interact. with Mater. Atoms* **2000**, *161–163*, 334–338. https://doi.org/10.1016/S0168-583X(99)00768-5.
(39) Campbell, J. L.; Cureatz, D. J. T.; Flannigan, E. L.; Heirwegh, C. M.; Maxwell, J. A.; Russell, J. L.; Taylor, S. M. The Guelph PIXE Software Package V. *Nucl. Instruments Methods Phys. Res. Sect. B Beam Interact. with Mater. Atoms* **2021**, *499*, 77–88. https://doi.org/10.1016/J.NIMB.2021.05.004.
(40) Barradas, N. P.; Jeynes, C. Advanced Physics and Algorithms in the IBA DataFurnace. *Nucl. Instruments Methods Phys. Res. Sect. B Beam Interact. with Mater. Atoms* **2008**, *266* (8), 1875–1879. https://doi.org/10.1016/J.NIMB.2007.10.044.
(41) Gurbich, A. *SigmaCalc 1.6*. http://www-nds.iaea.org/sigmacalc/.
(42) Barradas, N. P.; Alves, E.; Pereira, S.; Shvartsman, V. V.; Kholkin, A. L.; Pereira, E.; O'Donnell, K. P.; Liu, C.; Deatcher, C. J.; Watson, I. M.; Mayer, M. Roughness in GaN/InGaN Films and Multilayers Determined with Rutherford Backscattering. *Nucl. Instruments Methods Phys. Res. Sect. B Beam Interact. with Mater. Atoms* **2004**, *217* (3), 479–497. https://doi.org/10.1016/J.NIMB.2003.11.009.